Analyzing transport properties of p-type Mg_2Si-Mg_2Sn solid solutions: Optimization of thermoelectric performance and insight into the electronic band structure

H. Kamila[a*], P. Sahu[c], A. Sankhla[a], M. Yasseri[a,b], N. H. Pham[a], T. Dasgupta[c], E. Mueller[a,b], J. de Boor[a*]

[a] Institute of Materials Research, German Aerospace center, Linder Hoehe, Cologne 51147, Germany

[b] Institute of Inorganic and Analytical Chemistry, Justus Liebig University Giessen, Giessen 35392, Germany

[c] Department of Metallurgical Engineering and Materials Science, Indian Institute of Technology Bombay, Mumbai 400 076, India

Abstract

We have synthesized the complete stoichiometric range of the p-$Mg_2Si_{1-x}Sn_x$ striving for the optimization of the thermoelectric properties of p-type Mg_2(Si, Sn) with respect to composition. The experimental data is analyzed in the framework of a single parabolic band (SPB) model and we can show that the thermoelectric properties can be well presented if acoustic phonon scattering and alloy scattering are taken into account.

We find that the maximum achievable carrier concentration and power factor increase with higher Sn content. Also, the carrier mobility increases strongly from Mg_2Si to Mg_2Sn due to changing density of states effective mass for the valence band which decreases from $m_D^*\,(Mg_2Si) = 2.2\,m_0$ to $m_D^*(Mg_2Sn) = 1.1\,m_0$. Retrieval of the acoustic phonon scattering potential ($E_{Def} = 9\,eV$) and the alloy scattering parameter ($E_{AS} = 0.5\,eV$) allows modelling the thermoelectric properties for any arbitrary composition. Hence, we can predict the optimum zT for $x \approx 0.65 - 0.7$ and the maximum power factor for Sn-rich compositions. We furthermore reveal that significant improvement of the thermoelectric properties of Si-rich compositions can be achieved by increasing the carrier concentration experimentally and that the disparity between n- and p-type Mg_2(Si, Sn) is due to the differences between the valence and the conduction bands and not the interaction potentials.

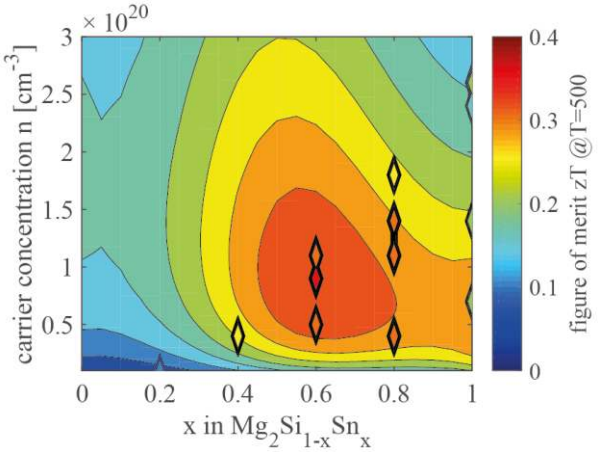

Introduction

Thermoelectric materials are very attractive because they can directly convert waste heat into electricity. Thermoelectric system have advantages such as small system size, no moving parts, heating and cooling in one system, environmental compatibility and high reliability. The development of thermoelectric generators (TEG) is promising for a wide range of divers applications, ranging from self-powering sensors, to waste heat recovery in the automotive sector and the steel industry to the powering of space probes [1, 2]. The efficiency of thermoelectric generators (TEG) depends on the figure of merit zT of the employed materials which is defined by $zT = \frac{S^2\sigma}{\kappa} T$ where S is the Seebeck coefficient, σ the electrical conductivity, κ the thermal conductivity, and T the temperature.

In recent years the field of thermoelectrics has made significant progress due to the development of efficient thermoelectric materials with high zT, these include nanostructured PbTe [3], $CoSb_3$-based Skutterudites [4], half-Heusler compounds [5], Zintl phases [6] and Mg_2Si-based solid solutions [7]. Among these, magnesium silicide based solid solutions (Mg_2X with X = Si, Sn) are promising for waste heat recovery in the mid-temperature range due to their environmental compatibility, low cost, abundance, and non-toxicity [8-10]. While n-type $Mg_2Si_{1-x}Sn_x$ has excellent thermoelectric properties ($zT \approx 1.4$) [11, 12], the p-type properties are clearly inferior [13]. However, both good and compatible n- and p-type materials are required to build TEG. Using n- and p- type from the same material class would be highly advantageous as this would simplify contact development and furthermore imply similar coefficient of thermal expansion, hence reducing thermomechanical stresses [14]. Therefore, optimizing p-type $Mg_2Si_{1-x}Sn_x$ is highly desired.

Previous works have reported on p-type $Mg_2Si_{1-x}Sn_x$ using Ag [15-20], Li [21-26], Ga [27, 28], and Na [29] as single dopants; a studying using double doping was also presented [30]. The highest zT_{max} of 0.7 has been reported for Li-doped samples [13, 23], possibly because of the high solubility of Li [13, 31]. A comparative study on the Mg_2Ge-Mg_2Sn system furthermore showed similar effective masses for samples doped with Li, Ga, and Na and indicated validity of the rigid band model for these dopants [32]. Among different compositions of Li-doped $Mg_2Si_{1-x}Sn_x$ with $x = 0 - 1$, the Sn-rich compositions ($0.6 \leq x \leq 0.8$) have good thermoelectric properties as for those it appears to be easier to obtain carrier concentrations close to the optimum one [21, 23, 24, 26].

de Boor et al. reviewed p-type Mg_2X [13] and hypothesized from the existing works that mobility increases with increasing Sn content and the density of states effective mass slightly decreases. However, the analyzed data were obtained using different synthesis techniques which makes the results difficult to compare as carrier mobilities are influenced by the synthesis route. Furthermore, the density of states effective mass has been analyzed in a relatively small compositional range. Till date, there has been no study determining the thermoelectric properties for the complete stoichiometric range of p-type $Mg_2Si_{1-x}Sn_x$ identifying the optimum composition for p-type $Mg_2(Si,Sn)$. Series of samples with a given x have been analyzed using a single parabolic band (SPB) model [21, 24, 26, 33-35]. However, no attempt has been made so far to model the whole solid solution nor have the fundamental

scattering parameters been estimated. Moreover, while theoretical works indicate significantly different curvatures of the valence bands in Mg_2Si and Mg_2Sn this has not been verified experimentally [36].

Here we prepared p-type Li doped $Mg_2Si_{1-x}Sn_x$ with $x = 0 - 1$ by high energy ball milling. All the samples properties were analyzed utilizing the SPB model. The temperature dependence of electrical conductivity/mobility is modeled with good agreement to the experimental data taking into account acoustic phonon (AP) scattering and alloy scattering (AS). Analysis of the data within the SPB model shows that the density of states effective mass decreases towards Mg_2Sn resulting in an optimum material for $x \approx 0.65 - 0.7$ coinciding with the experimental values. The maximum power factor is achieved for Sn-rich compositions. The calculations furthermore reveal that significant improvement of the thermoelectric properties of Si-rich composition can be obtained by increasing the carrier concentration experimentally. Direct comparison of fundamental material properties of n- and p-type $Mg_2(Si,Sn)$ indicates that the difference between conduction bands and valence bands is almost exclusively the reason for the inferior performance of p-type.

Materials and methods

P-type $Mg_{2-y}Li_ySi_{1-x}Sn_x$ (x = Sn content and y = Li content) was synthesized utilizing high energy ball milling and current assisted sintering. The detailed procedure is described in our previous report [37]. Since the optimum thermoelectric properties are expected to be around $Mg_2Si_{0.4}Sn_{0.6}$ [37], the Li concentration in $Mg_{2-y}Li_ySi_{0.4}Sn_{0.6}$ was varied ($y = 0.001, 0.002, 0.003, \text{and } 0.005$) to determine optimum dopant concentration and Li concentration is varied for Sn-rich ($x \geq 0.6$) compositions as well [23]. More samples with different Sn content ($x = 0 - 1$) were prepared to study the effect of Sn substitution.

The temperature dependent S and σ measurements were performed utilizing an in-house developed facility with a four-probe technique [38, 39]. The thermal diffusivity (α) of the pellets was obtained using a Netzsch LFA 427 apparatus. The thermal conductivity (κ) was calculated using the relation $\kappa = \alpha\rho C_p$, ρ and C_p are sample density and heat capacity in dependence of composition at constant pressure respectively. The C_p value was calculated from Dulong Petit limit for C_V^{DP}: $C_p = C_v^{DP} + \frac{9E_t^2 T}{\beta_T \rho}$, where $E_t = 1.4 \times 10^{-5} + 4 \times 10^{-6}x$ K^{-1} and $\beta_T = 1.6923 \times 10^{-11} + 7.106 \times 10^{-12}x$ Pa^{-1} are the linear coefficient of thermal expansion and isothermal compressibility in dependence of composition, respectively [40]; the density is given here by $\rho = 1.92 + 1.5x$ g/cm^3. The measurements were performed under Ar and He from 300 – 698 K. The room temperature Hall coefficient (R_H) for different samples was determined using in-house facility with a van der Pauw configuration under varying magnetic field of maximum 0.5 T [40, 41]. The Hall carrier concentration n_H was calculated from R_H assuming a single carrier type $n_H = \frac{1}{R_H \,.\, e}$ where e is the electronic charge. We specify the uncertainties for S, σ, κ, R_H for different samples as $\pm 5\%, \pm 5\%, \pm 8\%, \pm 10\%$ based on a comparison to the NIST low temperature standard for the Seebeck coefficient [42] and internal reference measurements on a high temperature

standard proposed in [43]. Our estimates are comparable to the numbers obtained in an international round robin test [44].

Results

Thermoelectric transport data of p-type $Mg_2Si_{1-x}Sn_x$

A list of samples with nominal composition and room temperature Hall carrier concentration (n_H), density of states effective mass (m_D^*), and Hall mobility (μ_H) is given in Table 1.

Table 1. Thermoelectric transport data for p-type $Mg_2Si_{1-x}Sn_x$, for samples with $\boldsymbol{x < 0.6}$ the carrier concentration was not large enough to employ a SPB model

Composition	n_H x10^{20} (cm^{-3})	m_D^*	μ_H (cm^2/Vs)
$Mg_{1.99}Li_{0.01}Si_{0.4}Sn_{0.6}$	0.51	1.45	28
$Mg_{1.98}Li_{0.02}Si_{0.4}Sn_{0.6}$	0.86	1.42	33
$Mg_{1.97}Li_{0.03}Si_{0.4}Sn_{0.6}$	1.01	1.53	24
$Mg_{1.95}Li_{0.05}Si_{0.4}Sn_{0.6}$	0.87	1.39	28
$Mg_{1.995}Li_{0.005}Si_{0.2}Sn_{0.8}$	0.36	1.01	67
$Mg_{1.99}Li_{0.01}Si_{0.2}Sn_{0.8}$	1.14	1.42	41
$Mg_{1.98}Li_{0.02}Si_{0.2}Sn_{0.8}$	1.36	1.18	49
$Mg_{1.97}Li_{0.03}Si_{0.2}Sn_{0.8}$	1.83	1.26	42
$Mg_{1.995}Li_{0.005}Sn$	0.67	0.95	122
$Mg_{1.99}Li_{0.01}Sn$	1.44	1.12	97
$Mg_{1.98}Li_{0.02}Sn$	2.37	1.17	77
$Mg_{1.97}Li_{0.03}Sn$	2.6	1.22	58

Fig. 1a shows that all samples with $Mg_{2-y}Li_ySi_{0.4}Sn_{0.6}$ exhibit a positive Seebeck coefficient corresponding to p-type conduction. The Seebeck coefficient decreases and electrical conductivity increases with increasing y for low Li concentrations. However, for $y > 0.02$ a further increase of the Li concentration does not lead to significant change to the electronic properties. The thermal excitation of minority carriers can be seen for the low doped samples ($y = 0.01$) when the curve of S starts to bend at lower temperature compared to the other samples. For comparable compositions, the samples have similar carrier concentration values compared to the values reported previously using the same synthesis method [24]. The maximum power factor (PF_{max}) achieved is 1.2 mW·m^{-1}K^{-2} at 650 K for $y = 0.02$. The highest PF and the low thermal conductivity lead to optimum experimental figure of merit (zT), which is around 0.54 ± 0.07 at 650 K. This is one of the highest zT amongst the reported studies [21, 23, 24].

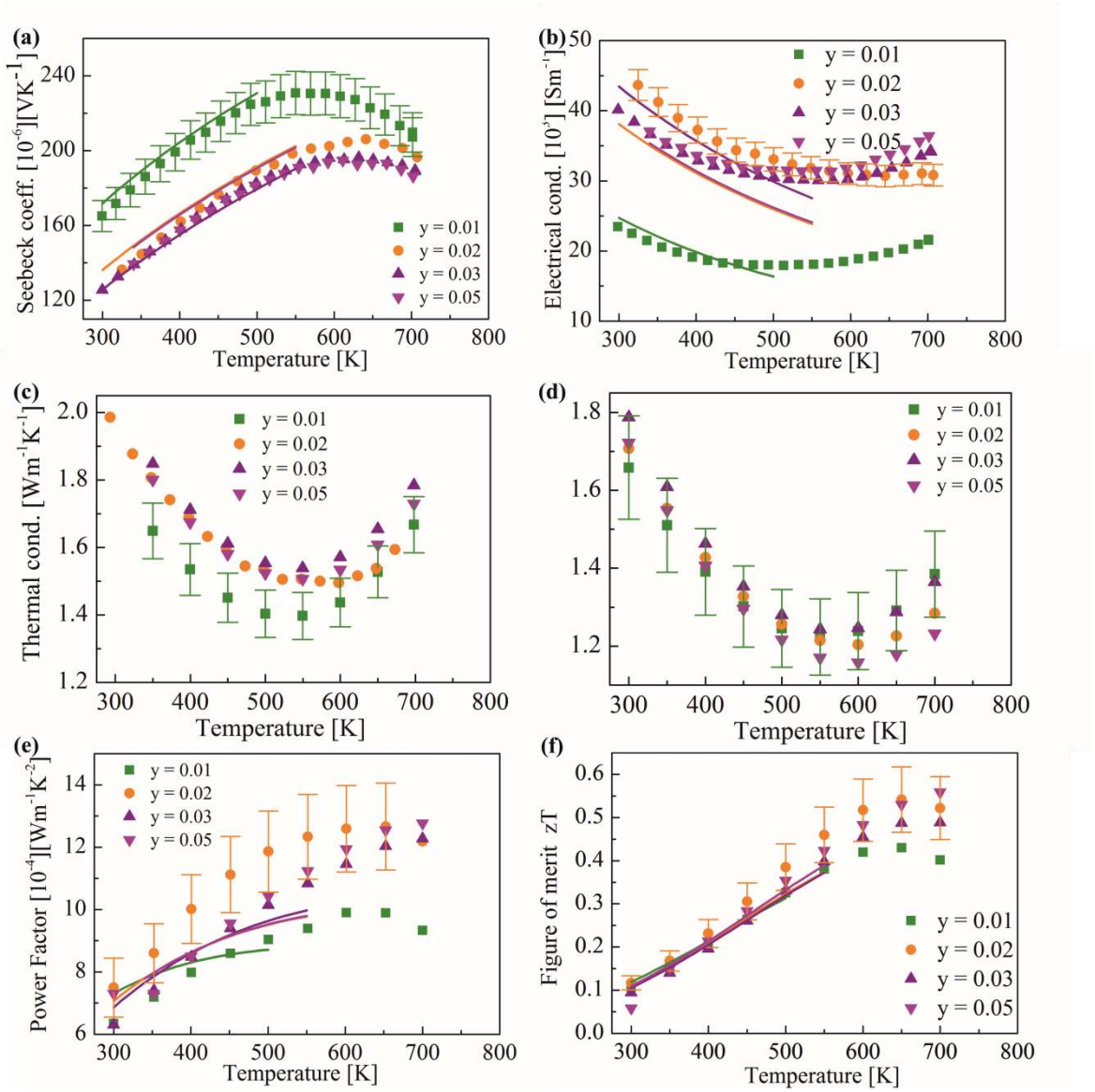

Fig. 1. Temperature dependent (a) Seebeck coefficient, (b) electrical conductivity, (c) power factor, (d) thermal conductivity, (e) lattice thermal conductivity, and (f) figure of merit for different Li concentration ($\boldsymbol{y = 0.01, 0.02, 0.03, and\ 0.05}$) for $Mg_{2-y}Si_{0.4}Sn_{0.6}$ with experimental data (symbols) and theoretical results based on the SPB model (lines).

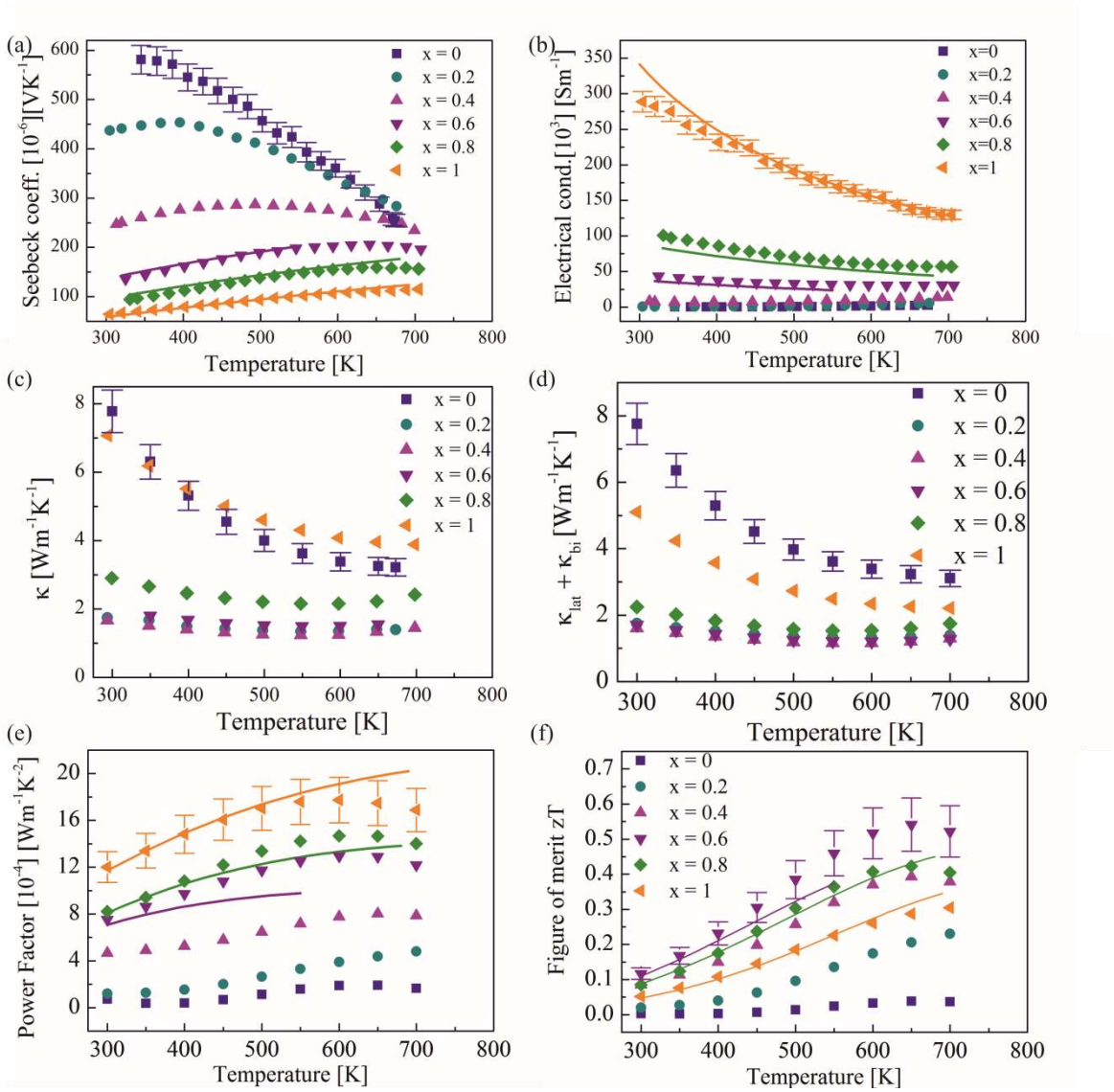

Fig. 2. Thermoelectric properties of $Mg_{1.98}Li_{0.02}Si_{1-x}Sn_x$ with $\boldsymbol{x = 0 - 1}$ (a) Temperature dependent Seebeck coefficient, (b) electrical conductivity, (c) thermal conductivity, (d) lattice thermal conductivity, (e) power factor, and (f) figure of merit $\boldsymbol{zT}$. Data points indicate experimental results and theoretical results are shown by lines based on single parabolic band (SPB) model for $\boldsymbol{x \geq 0.6}$.

From the data in Fig.2, the optimum experimental thermoelectric properties are obtained for $x = 0.6$ and $y = 0.02$. Furthermore, the Si:Sn ratio was varied to see the effect of Sn substitution on thermoelectric properties of $Mg_2Si_{1-x}Sn_x$ with $x = 0 - 1$. The obtained results show that the Seebeck coefficient gradually declines with increasing Sn content and the electrical conductivity rises dramatically. This is mainly because the carrier concentration and mobility increases with increase of Sn and Li contents (Table 1). The Seebeck coefficient curves of the Si-rich samples ($x \leq 0.4$) start to bend at low T due to thermal excitation of minority carriers. Si-rich samples have low carrier concentration in agreement with previous publications [22, 45]. The highest electrical conductivity is obtained for Mg_2Sn due to highest carrier concentration and mobility. This boosts the power factor (PF) values to 1.7 mW·m^{-1}K^{-2} at 600 K. The thermal conductivity drops by alloying Mg_2Si with Mg_2Sn and reaches the lowest value for $x = 0.6$ and $x = 0.4$. The figure of merit is thus highly dependent on Si:Sn

ratio due to the opposite effects on electronic and thermal properties. The Sn-rich compositions have higher values of zT than the Si-rich compositions.

Single Parabolic Band (SPB) analysis

The Single Parabolic Band model can be used for highly doped samples and has been employed for n- and p-type Mg_2X materials [21, 34, 35, 46]. It has been described in detail previously [47, 48]. The basic assumptions are that the electronic properties are governed by a single, parabolic, and rigid band i.e. the density of states effective mass is independent of carrier concentration and the band structure does not change with dopant substitution. The basic quantities of this model are the reduced chemical potential (η), the mobility parameter ($\boldsymbol{\mu_0}$) and the density of states effective mass ($\boldsymbol{m_D^*}$) [47], which are linked to each other and the measured transport quantities by the following equations:

$$S = \frac{k_b}{e}\left(\frac{2F_1}{F_0} - \boldsymbol{\eta}\right) \quad (1)$$

$$\boldsymbol{n} = 4\boldsymbol{\pi}\left(\frac{2m_D^* k_{b_B} T}{h^2}\right)^{1.5} \boldsymbol{F_{\frac{1}{2}}(\eta)} \quad (2)$$

$$\boldsymbol{n_H} = \frac{n}{r_H}, \boldsymbol{r_H} = \frac{1.5F_{0.5}(\eta)(0.5)F_{-0.5}(\eta)}{F_0^2(\eta)} \quad (3)$$

$$\boldsymbol{\mu_H} = \boldsymbol{\mu_0}\frac{F_{-0.5}(\eta)}{2F_0(\eta)} \quad (4)$$

$$\boldsymbol{\sigma} = \frac{\mu_H}{R_H} \quad (5)$$

Here k_b is Boltzmann's constant, $F_j(\eta)$ the Fermi integral of order i, and the reduced chemical potential η is given by $\eta = \frac{E_F}{k_b T}$, where E_F is Fermi energy. For the calculation, we have assumed a scattering parameter of $\lambda = 0$ corresponding to the energy dependence of scattering with AP and AS **[49, 50]**. The true carrier concentration n is obtained from the experimentally accessible Hall carrier concentration n_H by the Hall factor r_H. n refers to the carrier concentration in general while we use p when discussing hole concentrations. The density of states effective mass was calculated from n and η using eq. 1 and eq. 2. S vs. carrier concentration (Pisarenko plot) is shown in Fig. 3a for Sn-rich compositions together with literature data [21, 23-26, 30]. The density of states effective mass obtained for a given composition appears to increase slightly with increasing carrier concentration but the effect is small in the relevant carrier concentration range. We note that using a carrier concentration dependent effective mass instead of an average one would improve the fit between experimental and modelling data. However, further data on the effective mass would be required to have a sound physical basis for such a fit. Furthermore, the effect on the figure of merit is relatively small in the carrier concentration regime and conclusions that can be drawn from our results remain unchanged. Fig. 4b shows the dependence of our density of states effective mass on carrier concentration and composition in more detail. The average density of states effective mass of our samples are $1.1\ m_0$, $1.3\ m_0$, and $1.5\ m_0$ for $x = 1, 0.8,$ and 0.6 respectively, proving that replacing Si by Sn affects the band structure of p-type $Mg_2(Si,Sn)$. This is in agreement with the trends that have been calculated by Kutarosinski et al., who calculated the density of states effective mass for p-

Mg_2Si, Mg_2Ge, and Mg_2Sn from first principles. They showed that m_D^* is larger for Mg_2Si than for Mg_2Sn [36].

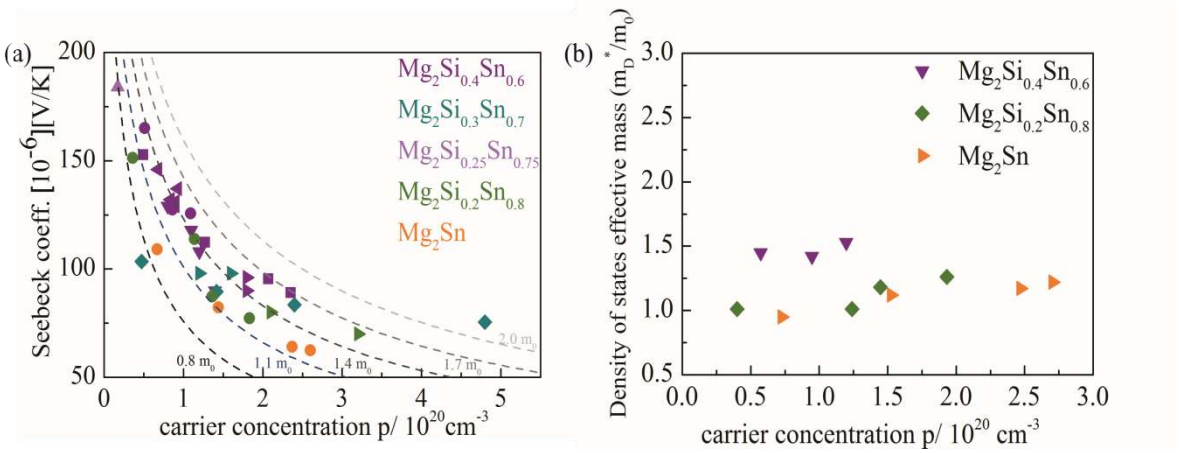

Fig. 3 (a) Seebeck coefficient at room temperature S(p) (The data were taken from from o this work, ∇ Gao et al. [23], Δ Isoda et al. [12], ◅ de Boor et al. [24], ▻ Isachenko et al. [25], ◇ Zhang et al. [21], and □ Tang et al. [26]) with m_D^* between 0.8-2.0 m_0 and (b) the dependence of m_D^* on carrier concentration and composition for the samples synthesized in this study.

Modeling of the thermoelectric properties of Mg_2X (X = Si, Sn)

A SPB model is usually employed to analyze the properties of a certain thermoelectric material (e.g. p-$Mg_2Si_{0.4}Sn_{0.6}$) with η, μ_0(T) and m_D^* as basic variables; $\kappa_L(T)$ is used as further input to be able to calculate zT. Here we use the experimental data to expand this model to cover the whole solid solution range of p-Mg_2(Si,Sn). To be able to do so, we need to obtain $\mu_0(T,x)$, $\kappa_L(T,x)$, and $m_D^*(x)$. As the SPB model is a description of the electronic transport only and lattice thermal conductivity is only an input parameter we have used polynomial fits (the fourth degree polynomial for T and the third degree polynomial for x) for the lattice thermal conductivity as a function of composition, see Fig. 4a. The lattice thermal conductivity was obtained from the measured thermal conductivity $\kappa_{lat} + \kappa_{bi} = \kappa - \kappa_e = \kappa - L\sigma T$, where the Lorenz number was calculated from $L = \left(\frac{k_b}{e}\right)^2 \frac{3F_0(\eta)F_2(\eta) - 4F_1{}^2}{F_0(\eta)^2}$ using the chemical potential of the samples (eq. 1). Restricting the data to the temperature range where the SPB is valid (see Fig. S1 (electronic supplementary information)) we ensure that the bipolar contribution κ_{bi} remains small. Our data on the lattice thermal conductivity shows the same trends with respect to composition and temperature as previous studies and the absolute values agree reasonably well [7, 51-53]

The experimental results for m_D^* shown in Fig. 4b were used as base for $m_D^*(x)$. As it was not possible to synthesize Si-rich samples without mixed conduction we have employed the $m_{D,p}^* = 2.2$ for $x = 0$ in agreement with earlier work [16, 54]. A similar value is also obtained if the mobility ratio $b = \frac{\mu_n}{\mu_p} \approx 6$ from the work from Zaitsev et al. is used to estimate the hole effective mass $\frac{m_{n,i}}{m_{p,i}} \approx \left(\frac{\mu_p}{\mu_n}\right)^{\frac{2}{5}} \left(\frac{E_{Def,p}}{E_{Def,n}}\right)^{4/5}$. Here we have used $m_{D,n}^* = 1.1\ m_0$ as reported by Bux et al. [33], in reasonable agreement with other reports [55, 56]. For arbitrary x $m_{D,P}^* = 2.2 - 1.1x$ which is a very good representation of the available

experimental data. As a result, the effective mass decreases from 2.2 m_0 to 1.1 m_0 as we move from Mg_2Si to Mg_2Sn (Fig. 4b).

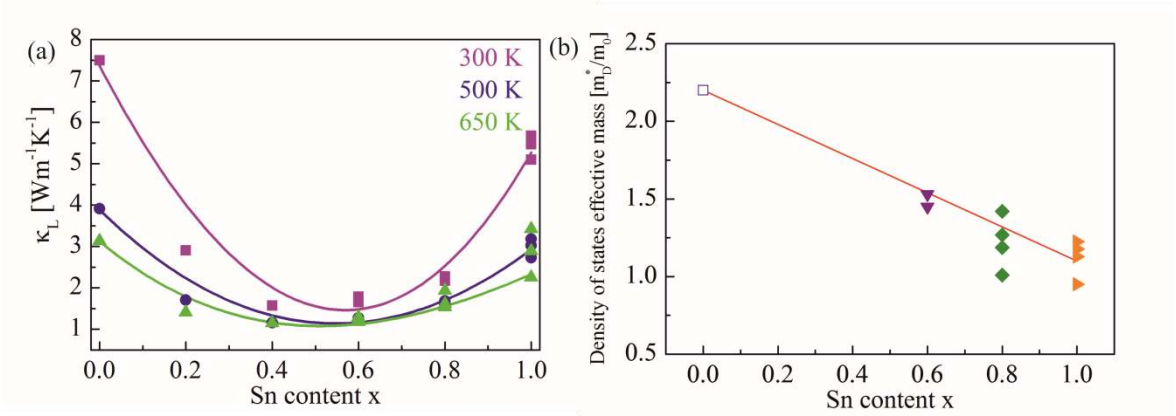

Fig. 4. (a) The lattice thermal conductivity vs Sn content from $\boldsymbol{x = 0 - 1}$ at 300, 500 and 650 K. Data points were obtained from measurements while the fitting is shown by lines. (b) The density of states effective mass vs Sn content: experimental results (filled symbols), literature data (empty symbol) and interpolating line.

The dependence of μ_0 and μ_H on temperature and composition was modeled taking acoustic phonon (AP) and alloy scattering (AS) into account. Acoustic phonon scattering is the most relevant scattering mechanism for highly doped samples at high temperatures [57]. Alloy scattering is included as it is a mechanism relevant in solid solutions [50]. AP leads to a temperature dependence $\mu_H^{AP} \sim T^{-z}$ with $z > 1$ [55] while the alloy scattering $\mu_H^{AS} \sim T^0$ [34]. We assume that the scattering mechanisms are independent of each other, hence the mobilities add inversely (Matthiessen's rule) [34]:

$$\frac{\mathbf{1}}{\boldsymbol{\mu_H}} = \frac{\mathbf{1}}{\boldsymbol{\mu_H^{AP}}} + \frac{\mathbf{1}}{\boldsymbol{\mu_H^{AS}}} \tag{6}$$

The mobility for acoustic phonon scattering can be described by [57, 58]:

$$\boldsymbol{\mu_H^{AP}} = \frac{\sqrt{8\pi} e \hbar^4 \rho v_l^2 \psi(\eta)}{3 E_{Def}^2 (m_s)^{2.5} (k_b T)^{1.5}} \tag{7}$$

where $\hbar$ is the reduced Planck constant, k_b is Boltzmann's constant, ρ is the theoretical mass density, v_l is the longitudinal velocity of sound, E_{Def} is deformation potential which characterizes the interaction between charge carriers and phonons, and $\psi(\eta) = \frac{3\sqrt{\pi}}{4}\frac{0.5}{2}\frac{F_{-0,5}(\eta)}{F_0(\eta)}$ is a combination of constants and Fermi integrals that can be calculated from η. The longitudinal velocity of sound of Mg_2Si [59], Mg_2Sn [60], $Mg_2Si_{0.4}Sn_{0.6}$ [61], and $Mg_2Si_{0.3}Sn_{0.7}$ [34] were taken from different literature while the velocity for other composition were calculated by linear interpolation ($v_l = 7680 - 2880x$). The single valley effective mass m_s^* was obtained from $m_D^* = N_v^{2/3} m_s^*$ with $N_v = 2$, where N_v is valley degeneracy. $Mg_2(Si,Sn)$ has in principle 3 valence bands at the Γ point (light hole (LH), heavy hole (HH), split off (SO)), however detailed calculations show that the influence of the split-off band is small [36]. The LH and HH are supposed to have different curvatures so the m_s^* calculated in the chosen approach is the averaged single valley effective mass of both bands, a simplification in the boundaries of the SPB model that has been employed previously [34].

For Mg_2Sn, AP scattering is expected to be the dominant scattering mechanism. Employing eq. 6 and eq. 7, the estimated value of E_{Def} = 9 eV was obtained by fitting μ_H^{AP} (orange dashed line) to the experimental μ_H (orange solid line), which can be seen in Fig. 5a. It can be seen that the temperature dependence is captured well, but not perfectly, probably due to the influence of additional scattering mechanisms such as grain boundary (GB) scattering and ionized impurities [34, 55]. The value of $E_{Def}(9\ eV)$ of p-Mg_2Sn is comparable, but slightly lower than what has been reported for n-type Mg_2Si [55]. The E_{Def} value of p-Mg_2Sn is lower than for p-PbTe, p-PbSe, p-Bi_2Te_3, and p-$CoSb_3$ [62] and comparable to the reported estimates of E_{Def} for n-$Mg_2Si_{0.3}Sn_{0.7}$ [34], n-type $Mg_2Si_{0.45}Sn_{0.55}$ [35], and p-$Ca_{0.99}Na_{0.01}Mg_2Sb_2$ [63]. A low deformation potential corresponds to the weak interaction between the holes and phonons [57]. Weak interaction leads to higher carrier mobility and good TE properties [34, 57].

The alloy scattering parameter E_{AS} can be obtained by fitting the experimental μ_H for $x \neq 1$ to eq. 6, with the mobility due to alloy scattering given by:

$$\boldsymbol{\mu_H^{AS} = \frac{64e\hbar^4 N_0 \psi(\eta)}{9(2\pi)^{1.5} x(1-x) E_{AS}^2 (m_s)^{2.5} (k_b T)^{0.5}}} \quad (8)$$

where N_0 is the number of atoms per unit volume and x is Sn fraction, respectively. We have kept $E_{Def} = const = 9\ eV$ for all compositions. The validity of our approach this was tested by simultaneously fitting E_{Def} and E_{AS} to the data for all compositions with $x = 0.6$ which yield $E_{Def} = 9\ eV$ and $E_{AS} = 0.5\ eV$. Note that Bahk et al. modeled the deformation potential as a parabolic function of Sn content x [64]. This was presumably done to account implicitly for alloy scattering while in this work it was taken into account explicitly. E_{AS} is independent of x with the value depending on the alloy components such as Mg_2Sn and Mg_2Si or Mg_2Ge and Mg_2Sn [50]. Best agreement for all compositions was found for $E_{AS} = 0.5\ eV$. The alloy scattering parameter is typically between 0.6 to 2 eV for thermoelectric materials [49]. A rough estimation of the alloy scattering parameter can be obtained by taking into account the difference in the band gap values of the components of solid-solutions (for example: Mg_2Si (0.8 eV) and Mg_2Sn (0.4 eV) in the present case.) [50]. If we compare our result with the previous report on n-type $Mg_2Si_{0.45}Sn_{0.55}$, our value is in between 0.32 eV [34] and 0.7 eV [35]. The difference arises possibly due to additional scattering mechanism such as GB scattering [55] and the interplay between E_{AS} and E_{Def} that were chosen differently in the mentioned references [34, 35]. Fig. 5a shows the experimental μ_H and calculated μ_H^{AP}, and μ_H^{AS} using $Mg_2Si_{0.4}Sn_{0.6}$ as example. AS is the dominant scattering mechanism for $x = 0.6$ at room temperature and AP scattering is more important at high temperature. Fig. 5b shows $\mu_0(x)$ at different temperatures. The data was calculated using the E_{Def} and E_{AS} as input to obtain μ_0^{AP}, μ_0^{AS}, and μ_0 using Matthiessen's rule [34]. $\mu_0(x)$ appears as tilted parabola due to the superposition of the $x(1-x)$ dependence from AS (eq. 8) and the pronounced change with the effective mass ($\mu \sim {m_D^*}^{-2.5}$); the mobility therefore strongly increases for $x \geq 0.6$. The Mg_2Si-Mg_2Sn system exhibits thus a distinctly different trend than solid solutions of PbTe/PbSe [49] and $CaZn_2Sb_2$/$CaMg_2Sb_2$ [63]. The density of states effective mass of p-type $Mg_2(Si,Sn)$ decreases substantially with higher Sn content while in solid solution of PbTe/PbSe it remains constant [49].

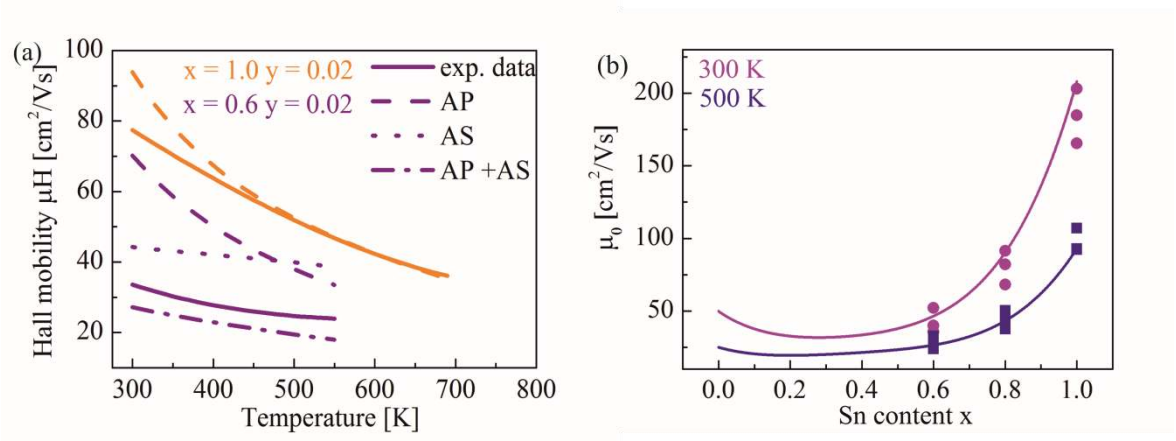

Fig. 5 (a) Temperature dependent hall mobility of $Mg_{2-y}Li_ySi_{1-x}Sn_x$ for $\boldsymbol{x = 0.6, 1}$ (solid lines). The individual mobilities due to AP, AS, and combined are shown as dashed, dotted, dashed-dotted lines, respectively. (b) The mobility parameter exhibits a strong dependence on $\boldsymbol{x}$ and a pronounced asymmetry.

Having obtained $\mu_0(T,x)$, $\kappa_L(T,x)$, and $m_D^*(x)$ the properties of the synthesized samples can be reproduced using eq. 1-6. Fig. 1 and Fig. 2 show good agreement between theoretical and experimental data. The samples properties were essentially reproduced by the model. The observed differences between the experimental data and the SPB prediction are mainly due to the usage of an averaged valued for m_D^* for samples of the same x. Note also that μ and hence σ have a stronger dependence on m_D^* than S, therefore fluctuation between the samples are more visible in the electrical conductivity data. Given that the model is based on very few input parameters ($E_{Def}, E_{AS}, \kappa_{lat}(T,x), m_D^*(x)$ and η as variable) it works very well to describe the thermoelectric properties of the complete solid solution.

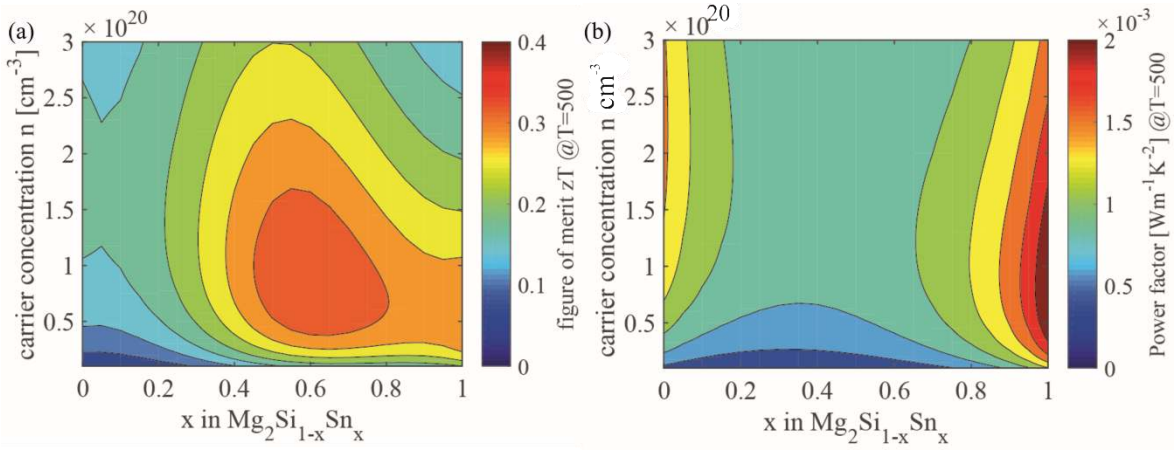

Fig. 6 (a) Figure of merit ($\boldsymbol{zT}$) and (b) power factor ($\boldsymbol{PF}$) mapping of p-type $Mg_2Si_{1-x}Sn_x$ with respect to the carrier concentration at 500 K.

The modelling results for $zT(n,x)$ and $PF(n,x)$ at 500 K are presented in Fig. 6. This temperature is chosen because the influence of the minority carriers is relevant in small interval (see Fig. S1 (electronic supplementary information)). Two experimental key parameters can be obtained from this: the Si:Sn ratio x_{opt} with the best properties and the optimum carrier concentration p_{opt}. The zT mapping shows that the optimum zT (~0.4) can be achieved for $x_{opt} = 0.6 - 0.7$ at 500 K for $p_{opt} \approx 8 \times 10^{20} cm^{-3}$. This is in agreement with the existing experimental works. For the Si-rich compositions $(x \leq 0.4)$, the figure of

merit is lower than the Sn-rich compositions ($x \geq 0.6$). Note that a significant improvement of thermoelectric properties of Si-rich composition beyond the currently achieved values is possible if the carrier concentration is experimentally increased, e.g. by double doping or different synthesis method approaches. The Si-rich compositions have higher thermal stability than Sn-rich composition which makes them preferential for higher application temperatures. The highest PF can be obtained for the binary end members with Mg_2Sn showing the best values.

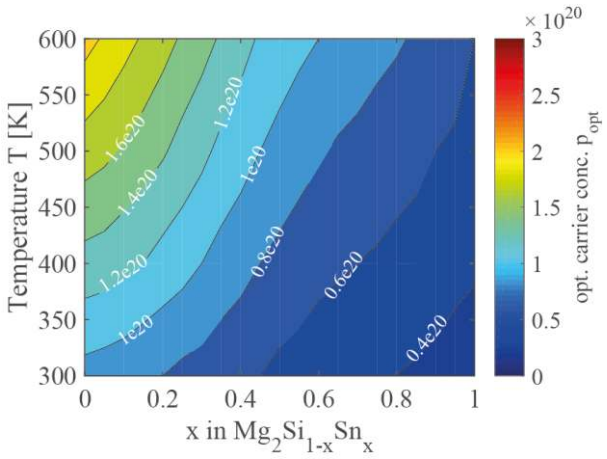

Fig. 7 Optimum carrier concentration mapping of p-type $Mg_2Si_{1-x}Sn_x$ with respect to temperature.

Fig. 7 shows the dependence of the optimum carrier concentration p_{opt} of p-type $Mg_2Si_{1-x}Sn_x$ with respect to temperature and composition. The optimum carrier concentration that gives the highest zT increases significantly with temperature, so for the typical application case with a large temperature gradient a compromise or a functionally graded material has to be employed [65]. The influence of the minority carriers limits the predictive power at high temperature, however the same trend has also been found for multiband modelling studies [66]. With respect to composition a trend towards lower p_{opt} with increasing x is clearly visible. This is mainly due to the decrease of $m_D^*(x)$ with increasing x. The decreasing band gap from Mg_2Si to Mg_2Sn will partially compensate this dependence for higher temperatures if more than one band is considered.

Discussion

The experimental results of this work cannot be compared directly to other publications. First because this is the first work that covers the whole compositional range of p- Mg_2Si-Mg_2Sn and second because the "fundamental" material parameters μ_0 and κ_{lat} are influenced by the microstructure and thus to some degree depend on the synthesis route chosen. However, the reported thermoelectric properties are in qualitative agreement with previous reports on certain compositions [34, 35, 55] and the obtained trends on e.g. mobility and effective mass are in agreement with what has been inferred from summarizing earlier literature data [13]. Our results agree qualitatively with multiband calculations from Satyala and Vashaee in the point that the optimum charge carrier concentration for p- Mg_2Si is much larger than that of corresponding n-type and that it is well above $10^{20} cm^{-3}$ [67]. Bahk et al. used multiband approach to calculate the thermoelectric properties of n- and p- $Mg_2(Si,Sn)$ considering also multiple scattering mechanisms [64]. The results of their much more complex model agree

qualitatively with ours but their modelling of the p-type was based on very limited experimental data and they did not capture the change of band structure with composition.

The results of our analysis can be used to understand why p-type $Mg_2(Si,Sn)$ shows inferior properties than the corresponding n-type. The thermoelectric figure of merit can be written as $zT = \frac{S^2}{L+(\psi\beta)^{-1}}$ with $\psi = \frac{8\pi e}{3}\left(\frac{2m_0k_b}{h^2}\right)^{1.5}F_0$ and the material parameter $\beta = \frac{\left(\frac{m_D^*}{m_0}\right)^{1.5}\mu_0}{\kappa_L}$ can be used to evaluate the performance of thermoelectric materials [47]. The mobility μ_0 decreases with increasing scattering potentials E_{Def} and E_{AS}, furthermore $\mu_0 \sim m_s^{*-2.5}$ for both AP and AS if m_s^* and the inertia mass are similar. The density of states effective mass is related to the single band effective mass by $m_D^* = N_v^{2/3}m_s^*$ with the valley degeneracy N_v. Good thermoelectric properties therefore require low scattering potential, a low m_s^*, but high m_D^* through large N_v.

These properties are listed in Table 2 for n- and p- binary Mg_2Si and $Mg_2Si_{0.4}Sn_{0.6}$ where the best properties are reported. Results from different papers show some scatter but it is clear that the scattering potentials are similar for n- and p- type; the main difference in performance thus comes from the density of states effective masses. For p-type Mg_2X $N_v = 2$ for all compositions while for n-type $N_v = 3$ for all compositions except $x = 0.6 - 0.7$ where the two conduction bands are converged and thus $N_v = 6$ [34, 51, 68]. Binary p- Mg_2Si has thus a much higher m_s^* and a smaller N_v than the n-type. For the solid solutions m_s^* is similar for both but the convergence of conduction bands favors the n-type significantly over the p-type. Note that p- Mg_2X does in fact not have two generated bands but two bands with different effective masses. The given m_s^* within the SPB corresponds to the averaged mass for the hypothetical case that the bands were indeed degenerate. This does, however, not influence the validity of the conclusions.

Table 2 The deformation potential and other parameters for n- and p- binary Mg_2Si and $Mg_2Si_{0.4}Sn_{0.6}$

Parameters	n-Mg_2Si	p-Mg_2Si	n-$Mg_2Si_{1-x}Sn_x$ ($x \approx 0.6$)	p-$Mg_2Si_{1-x}Sn_x$ ($x \approx 0.6$)	Ref.
E_{Def} [eV]	15, 17	9*	13, 8.77-9.34	9*	[35, 55], [64], [34, 35]
E_{AS} [eV]			0.7, 0.32-0.39	0.5*	[34, 35]
m_D^* [m_0]	1.1, 0.8	2.2*	2.3, 2.6	1.5, 1.3-1.5*	[33, 55],[16, 64, 67], [34, 69], [24]
m_s^* [m_0]	0.4-0.55	1.4	0.7-0.8	0.8-0.9*	*This work

Conclusion

We have successfully synthesized Li-doped p-type $Mg_2Si_{1-x}Sn_x$ with $x = 0, 0.2, 0.4, 0.6, 0.8, 1$ and determined the thermoelectric properties. We find that the thermoelectric properties of the whole solid solution can be well represented using a single parabolic band model taking into account acoustic phonon scattering and alloy scattering. The analysis furthermore yields

relatively low (and favorable) values for the deformation potential (9 eV) and the alloy scattering potential (0.5 eV). We can also show a significant decrease of the hole effective mass with increasing x in $Mg_2Si_{1-x}Sn_x$, favoring Sn-rich compositions and leading to an optimum material zT for $x \approx 0.65 - 0.7$ in agreement with our experimental findings. A significant improvement of the thermoelectric properties of Si-rich compositions is predicted if the carrier concentrations are increased beyond current experimental values.

Acknowledgements

We would like to gratefully acknowledge the endorsement from the DLR Executive Board Member for Space Research and Technology and the financial support from the Young Research Group Leader Program. The authors would like to thank to P. Blaschkewitz (DLR) for his untiring support with the thermoelectric measurement. The authors acknowledge Nader Farahi and Gagan K. Goyal for the fruitful discussion. The authors (H.K. and A.S.) would like to acknowledge financial support by the DAAD (Fellowships 247). The authors (H.K. and P.S.) would like to acknowledge collaboration financial support by DAAD-DST. Also, financial support of one of the authors (M.Y.) is provided by DFG via GRK (Research Training Group) 2204 “Substitute Materials for Sustainable Energy Technologies”.

References

[1] L.E. Bell, Science 321 (2008) 1457-1461.
[2] G.J. Snyder, E.S. Toberer, Nature Materials 7 (2008) 105.
[3] X. Hu, P. Jood, M. Ohta, M. Kunii, K. Nagase, H. Nishiate, M.G. Kanatzidis, A. Yamamoto, Energy & Environmental Science 9 (2016) 517-529.
[4] Y. Qiu, L. Xi, X. Shi, P. Qiu, W. Zhang, L. Chen, J.R. Salvaor, J.Y. Cho, J. Yang, Y.-c. Chien, S.-w. Chen, Y. Tang, G.J. Snyder, Advanced Functional Materials 23 (2013) 3194-3203.
[5] X. Yan, G. Joshi, W. Liu, Y. Lan, H. Wang, S. Lee, J.W. Simonson, S.J. Poon, T.M. Tritt, G. Chen, Z.F. Ren, Nano Letters 11 (2011) 556-560.
[6] J. Zhang, L. Song, S.H. Pedersen, H. Yin, L.T. Hung, B.B. Iversen, Nature Communications 8 (2017) 13901.
[7] W. Liu, X. Tan, K. Yin, H. Liu, X. Tang, J. Shi, Q. Zhang, C. Uher, Physical Review Letters 108 (2012) 166601.
[8] S. LeBlanc, S.K. Yee, M.L. Scullin, C. Dames, K.E. Goodson, Renewable and Sustainable Energy Reviews 32 (2014) 313-327.
[9] M.W. Gaultois, T.D. Sparks, C.K.H. Borg, R. Seshadri, W.D. Bonificio, D.R. Clarke, Chemistry of Materials 25 (2013) 2911-2920.
[10] J. de Boor, T. Dasgupta, E. Mueller, Thermoelectric Properties of Magnesium Silicide Based Solid Solution and Higher Manganese Silicides, in : C. Uher (Ed.) Materials aspect of thermoelectricity, CRC press Taylor & Francis, 2016.
[11] V. Zaitsev, Thermoelectric Handbook Macro to Nano (2006).
[12] P. Gao, I. Berkun, R.D. Schmidt, M.F. Luzenski, X. Lu, P.B. Sarac, E.D. Case, T.P. Hogan, Journal of Electronic Materials 43 (2014) 1790-1803.
[13] J. de Boor, T. Dasgupta, U. Saparamadu, E. Mueller, Z.F. Ren, Materials Today Energy 4 (2017) 105-121.
[14] G. Rogl, L. Zhang, P. Rogl, A. Grytsiv, M. Falmbigl, D. Rajs, M. Kriegisch, H. Mueller, E. Bauer, J. Koppensteiner, W. Schranz, M. Zehetbauer, Z. Henkie, M.B. Maple, Journal of Applied Physics 107 (2010) 043507.
[15] X. Tang, Y. Zhang, Y. Zheng, K. Peng, T. Huang, X. Lu, G. Wang, S. Wang, X. Zhou, Applied Thermal Engineering 111 (2017) 1396-1400.
[16] M. Akasaka, T. Iida, A. Matsumoto, K. Yamanaka, Y. Takanashi, T. Imai, N. Hamada, Journal of Applied Physics 104 (2008) 013703.

[17] H.Y. Chen, N. Savvides, T. Dasgupta, C. Stiewe, E. Mueller, physica status solidi (a) 207 (2010) 2523-2531.
[18] S. Kim, B. Wiendlocha, H. Jin, J. Tobola, J.P. Heremans, Journal of Applied Physics 116 (2014) 153706.
[19] H.Y. Chen, N. Savvides, Journal of Electronic Materials 38 (2009) 1056-1060.
[20] A. Prytuliak, E. Godlewska, K. Mars, D. Berthebaud, Journal of Electronic Materials 43 (2014) 3746-3752.
[21] Q. Zhang, L. Cheng, W. Liu, Y. Zheng, X. Su, H. Chi, H. Liu, Y. Yan, X. Tang, C. Uher, Physical Chemistry Chemical Physics 16 (2014) 23576-23583.
[22] P. Nieroda, A. Kolezynski, M. Oszajca, J. Milczarek, K.T. Wojciechowski, Journal of Electronic Materials 45 (2016) 3418-3426.
[23] P. Gao, J.D. Davis, V.V. Poltavets, T.P. Hogan, Journal of Materials Chemistry C 4 (2016) 929-934.
[24] J. de Boor, U. Saparamadu, J. Mao, K. Dahal, E. Mueller, Z. Ren, Acta Materialia 120 (2016) 273-280.
[25] G.N. Isachenko, A.Y. Samunin, E.A. Gurieva, M.I. Fedorov, D.A. Pshenay-Severin, P.P. Konstantinov, M.D. Kamolova, Journal of Electronic Materials 45 (2016) 1982-1986.
[26] X. Tang, G. Wang, Y. Zheng, Y. Zhang, K. Peng, L. Guo, S. Wang, M. Zeng, J. Dai, G. Wang, X. Zhou, Scripta Materialia 115 (2016) 52-56.
[27] W. Liu, K. Yin, X. Su, H. Li, Y. Yan, X. Tang, C. Uher, Intermetallics 32 (2013) 352-361.
[28] H. Ihou-Mouko, C. Mercier, J. Tobola, G. Pont, H. Scherrer, Journal of Alloys and Compounds 509 (2011) 6503-6508.
[29] S. Tada, Y. Isoda, H. Udono, H. Fujiu, S. Kumagai, Y. Shinohara, Journal of Electronic Materials 43 (2014) 1580-1584.
[30] Y. Isoda, S. Tada, T. Nagai, H. Fujiu, Y. Shinohara, MATERIALS TRANSACTIONS 51 (2010) 868-871.
[31] D. Kevorkov, R. Schmid-Fetzer, F. Zhang, Journal of Phase Equilibria and Diffusion 25 (2004) 140-151.
[32] U. Saparamadu, J. de Boor, J. Mao, S. Song, F. Tian, W. Liu, Q. Zhang, Z. Ren, Acta Materialia 141 (2017) 154-162.
[33] S.K. Bux, M.T. Yeung, E.S. Toberer, G.J. Snyder, R.B. Kaner, J.-P. Fleurial, Journal of Materials Chemistry 21 (2011) 12259-12266.
[34] W. Liu, H. Chi, H. Sun, Q. Zhang, K. Yin, X. Tang, Q. Zhang, C. Uher, Physical Chemistry Chemical Physics 16 (2014) 6893-6897.
[35] X. Liu, Z. Tiejun, W. Heng, H. Lipeng, X. Hanhui, J. Guangyu, S.G. Jeffrey, Z. Xinbing, Advanced Energy Materials 3 (2013) 1238-1244.
[36] K. Kutorasinski, B. Wiendlocha, J. Tobola, S. Kaprzyk, Physical Review B 89 (2014) 115205.
[37] H. Kamila, A. Sankhla, M. Yasseri, N.P. Hoang, N. Farahi, E. Mueller, J. de Boor, Materials Today : Proceedings (Accepted).
[38] J. de Boor, C. Stiewe, P. Ziolkowski, T. Dasgupta, G. Karpinski, E. Lenz, F. Edler, E. Mueller, Journal of Electronic Materials 42 (2013) 1711-1718.
[39] J. de Boor, E. Mueller, Review of Scientific Instruments 84 (2013) 065102.
[40] K.A. Borup, J. de Boor, H. Wang, F. Drymiotis, F. Gascoin, X. Shi, L. Chen, M.I. Fedorov, E. Mueller, B.B. Iversen, G.J. Snyder, Energy & Environmental Science 8 (2015) 423-435.
[41] L.J.v.d. Pauw, Philips Res. Rep 13 (1958) 1-9.
[42] J. Martin, Review of Scientific Instruments 83 (2012) 065101.
[43] P. Ziolkowski, C. Stiewe, J. de Boor, I. Druschke, K. Zabrocki, F. Edler, S. Haupt, J. König, E. Mueller, Journal of Electronic Materials 46 (2017) 51-63.
[44] H. Wang, S. Bai, L. Chen, A. Cuenat, G. Joshi, H. Kleinke, J. König, H.W. Lee, J. Martin, M.-W. Oh, W.D. Porter, Z. Ren, J. Salvador, J. Sharp, P. Taylor, A.J. Thompson, Y.C. Tseng, Journal of Electronic Materials 44 (2015) 4482-4491.
[45] A. Kolezynski, P. Nieroda, K.T. Wojciechowski, Computational Materials Science 100 (2015) 84-88.
[46] J. de Boor, S. Gupta, H. Kolb, T. Dasgupta, E. Mueller, Journal of Materials Chemistry C 3 (2015) 10467-10475.

[47] A.F. May, High-temperature transport in lanthanum telluride and other modern thermoelectric materials, California Institute of Technology, 2010.
[48] A.F. May, G.J. Snyder, Materials, preparation, and characterization in thermoelectrics. CRC Press, Boca Raton 11 (2012).
[49] H. Wang, A.D. Lalonde, Y. Pei, G.J. Snyder, Advanced Functional Materials 23 (2013) 1586-1596.
[50] J. Harrison, J. Hauser, Physical Review B 13 (1976) 5347.
[51] V. Zaitsev, M. Fedorov, E. Gurieva, I. Eremin, P. Konstantinov, A.Y. Samunin, M. Vedernikov, Physical Review B 74 (2006) 045207.
[52] X.J. Tan, G.Q. Liu, H.Z. Shao, J.T. Xu, B. Yu, H.C. Jiang, J. Jiang, Applied Physics Letters 110 (2017) 143903.
[53] P. Bellanger, S. Gorsse, G. Bernard-Granger, C. Navone, A. Redjaimia, S. Vivès, Acta Materialia 95 (2015) 102-110.
[54] M. Heller, G. Danielson, Journal of Physics and Chemistry of Solids 23 (1962) 601-610.
[55] J. de Boor, T. Dasgupta, H. Kolb, C. Compere, K. Kelm, E. Mueller, Acta Materialia 77 (2014) 68-75.
[56] E.C. Stefanaki, G.S. Polymeris, M. Ioannou, E. Pavlidou, E. Hatzikraniotis, T. Kyratsi, K.M. Paraskevopoulos, Journal of Electronic Materials 45 (2016) 1900-1906.
[57] J. Bardeen, W. Shockley, Physical Review 80 (1950) 72-80.
[58] C. Herring, E. Vogt, Physical Review 105 (1957) 1933-1933.
[59] Magnesium silicide (Mg2Si) sound velocities, elastic moduli, in: O. Madelung, U. Rössler, M. Schulz (Eds.), Non-Tetrahedrally Bonded Elements and Binary Compounds I, Springer Berlin Heidelberg, Berlin, Heidelberg, 1998, pp. 1-4.
[60] Magnesium stannide (Mg2Sn) sound velocity, elastic moduli, in: O. Madelung, U. Rössler, M. Schulz (Eds.), Non-Tetrahedrally Bonded Elements and Binary Compounds I, Springer Berlin Heidelberg, Berlin, Heidelberg, 1998, pp. 1-4.
[61] T.-W. Fan, J.-L. Ke, L. Fu, B.-Y. Tang, L.-M. Peng, W.-J. Ding, Journal of Magnesium and Alloys 1 (2013) 163-168.
[62] K. Koumoto, T. Mori, Thermoelectric nanomaterials, Springer, 2015.
[63] M. Wood, U. Aydemir, S. Ohno, G.J. Snyder, Journal of Materials Chemistry A 6 (2018) 9437-9444.
[64] J.-H. Bahk, Z. Bian, A. Shakouri, Physical Review B 89 (2014) 075204.
[65] E. Mueller, Č. Drašar, J. Schilz, W. Kaysser, Materials Science and Engineering: A 362 (2003) 17-39.
[66] K. Kutorasinski, J. Tobola, S. Kaprzyk, Physical Review B 87 (2013).
[67] N. Satyala, D. Vashaee, Journal of Electronic Materials 41 (2012) 1785-1791.
[68] T. Dasgupta, C. Stiewe, J. de Boor, E. Mueller, physica status solidi (a) 211 (2014) 1250-1254.
[69] A. Sankhla, A. Patil, H. Kamila, M. Yasseri, N. Farahi, E. Mueller, J. de Boor, ACS Applied Energy Materials 1 (2018) 531-542.